SOFT ROBOTICS
Volume 9, Number 6, 2022

DOI: 10.1089/soro.2021.0074

SoRo
Soft Robotics

ORIGINAL ARTICLE

3D-Printed Soft Sensors for Adaptive Sensing with Online and Offline Tunable Stiffness

Liang He,[1] Nicolas Herzig,[2] Thrishantha Nanayakkara,[3] and Perla Maiolino[1]

Abstract

The stiffness of a soft robot with structural cavities can be regulated by controlling the pressure of a fluid to render predictable changes in mechanical properties. When the soft robot interacts with the environment, the mediating fluid can also be considered an inherent information pathway for sensing. This approach to using structural tuning to improve the efficacy of a sensing task with specific states has not yet been well studied. A tunable stiffness soft sensor also renders task-relevant contact dynamics in soft robotic manipulation tasks. This article proposes a type of adaptive soft sensor that can be directly three-dimensional printed and controlled using pneumatic pressure. The tunability of such a sensor helps to adjust the sensing characteristics to better capturing specific tactile features, demonstrated by detecting texture with different frequencies. We present the design, modeling, Finite Element Simulation, and experimental characterization of a single unit of such a tunable stiffness sensor. How the sensing characteristics are affected by adjusting its stiffness is studied in depth. In addition to the tunability, the results show that such types of adaptive sensors exhibit good sensitivity (up to 2.6 KPa/N), high sensor repeatability (average std <0.008 KPa/N), low hysteresis (<6%), and good manufacturing repeatability (average std = 0.0662 KPa/N).

Keywords: soft sensing, 3D printed soft sensors, active sensing, tunable stiffness sensors

Introduction

The information acquired through the tactile sensors allows the robot to estimate relevant states to perform delicate tasks and to deal with uncertainties.[1] Research studies have been done extensively to replicate the sense of human touch in an artificial system[1,2] with approaches such as capacitive,[3] piezoelectric,[4] piezo-resistive,[5] and optical[6] sensors. Recently, the growing attention to unstructured soft interaction also raises the interest in developing soft tactile sensors that can undertake large deformation.[7]

Manufacturing sensors that are as soft as human tissue is challenging due to the limitation of the softness of the transducers.[1] High softness normally introduces high hysteresis and creep of the sensors.[8] To some degree, sensors based on computer vision can overcome such limitations.[9] However, those sensors are facing difficulties in complex contact modeling, limited sampling rate, constraint

[1]Oxford Robotics Institute, University of Oxford, Oxford, United Kingdom.
[2]Department of Engineering and Design, School of Engineering and Informatics, University of Sussex, Brighton, United Kingdom.
[3]Dyson School of Design Engineering, Imperial College London, London, United Kingdom.

geometry, and size. Another critical factor limiting the application of soft tactile sensors is their adaptability and robustness when interacting with unstructured environments.[10] A tactile sensor can be very sensitive for a particular low-force range but easily saturate and damage when there is an unexpected high force.[3]

Thus, this article proposes a soft but stiffness-controllable sensor driven by pressurized air. The compressible media air allows the sensor to be extremely soft. Moreover, the sensor's stiffness, sensing range, and sensitivity are controlled by the driving pressure to match the specific task requirements.

Actuation and perception can be considered as an integration.[10,11] When an object interacts with the environment, the tactile measurements ultimately depend on the sensor configurations, especially in soft sensors. In other words, the physical property of the sensor/agent acts as a physical reservoir that filters the tactile information for active sensing. Such integration of perception and actuation is widely seen in nature. For instance, humans change finger stiffness and behavior to maximize the gained tactile information for haptic explorations.[12] The active change of joint impedance helps humans maintain safe interaction in high uncertainty tasks and high precision in a more constructed environment. The ability to vary the stiffness allows haptic information to be processed with various interaction modalities for state optimization.[13]

Analogy, the mice, and rats also modulate their whisker movement to perform active sensing according to a specific environment by elaborately controlling the muscle of the follicle to bias the range of sensing from low to high frequencies.[14] Incorporating actuation in perception shows a new trend to develop robotic counterparts to understand the environment more effectively.[11] Another example can be found in active haptic exploration to localize a nodule in soft tissue with a tunable-stiffness robotic probe.[15] Examining the tissue with different stiffness of the probe can significantly reduce the uncertainty of the measured haptic information, thus, more effective in the detection.

While previous development of active sensing predominately relies on the stiffness and action change of the agent where the tactile sensor is mounted on a probe, coupled actuation and perception can also be incorporated in the sensor design itself.[10] This approach is particularly useful, considering that many robots interact with the environment directly with tactile sensors.

The ability to change the characteristics of the soft sensor itself introduces three significant advantages. First, it can favor the sensing region actively. A similar example can be found in cameras that can change the focus. Second, it can enable sensing with different sensitivities without the need to use different sensors.[16] Tactile information can be unreliable when the contact is soft with large hysteresis. Sensing multiple iterations with different sensitivities would ultimately increase the confidence level. Third, it can activate active sensing where the sensor can enable different interaction models by changing the contact stiffness. The mechanical property change can introduce a filtering effect of environmental noise and simplify further inference in information clustering.[17]

The proposed adaptive soft tactile sensor (Fig. 1) presents tunable stiffness and controllable sensing characteristics for active sensing. The approach allows the sensors to be directly three-dimensional (3D) printed with rubber-like materials and a further adjustment on the compliance with internal driving pressure. The online sensing characteristic change during the adjustment improves the efficacy of a sensing task with specific states. The tunability enabled a single sensor to interact with an object with different contact dynamics. The mechanical and associate sensing behavior changes are characterized in this article by theoretical modeling, finite element simulation, and experiments.

We compared the performance and analyzed the effect of material stiffness on sensing. Two-mode of sensor stiffness control can be achieved (1) offline-stage where the stiffness of the sensor can be changed using multimaterial 3D printing; (2) online-stage where sensor physical properties are changed by tuning the internal fluid pressure. A texture detection experiment is included to show the advantage of having a tunable sensor, with results indicating that a single sensor can be favored in detecting various textures by controlling its stiffness. In general, results show that this methodology developed tunable-stiffness sensors with good sensitivity (up to 2.6 KPa/N), high sensor repeatability (average std <0.008 KPa/N), low hysteresis (<6%), and good manufacturing repeatability (average std = 0.0662 KPa/N of 6 groups of 18 samples).

Design and Modeling

Basic structure and working mechanism of the tunable stiffness soft sensor

When a soft sensor actively interacts with a solid object, both agents are subjected to external forces with deformation associated with internal stresses and strains. Unlike soft sensors with fixed features, where the material properties are only characterized as the parameter to determine absolute sensor responses,[18] the proposed tunable stiffness sensor determines the sensing model based on the physical property. This active sensing framework is demonstrated by exploring the inherited sensing characteristics with pressurized fluid,[19] where significant sensing characteristics and stiffness change are exhibited during inflation.

The proposed sensor incorporates a 3D printed soft membrane to form a closed cavity that can be pressurized through an air source (Fig. 1). Rubber-like materials with the PolyJet 3D-printing technique introduced controllable membrane stiffness in the design phase (Object-260). Deformation of the soft architecture is triggered when an external force is applied to the soft membrane. According to Boyle's law, such changes in the cavity volume will be reflected using the pressure variation. Thus, the pressure variation reflects the exerted force between the tactile sensors and the environment.

In addition, the sensor's mechanical properties and sensing characteristics are controlled by the internal pressure. The sensor exhibits different interaction models to the environment depending on whether it is soft (low driving pressure) or stiff (high driving pressure). Two parameters for regulating the sensor stiffness are defined as (1) the offline parameter membrane stiffness (Tango+ and Digital materials [DM], see Table 1 and Supplementary Data A)[23,24] and (2) the online parameter internal driving pressure.

Theoretical modeling

The sensor is modeled under the assumption of a hyperelastic membrane using three different states depending on its

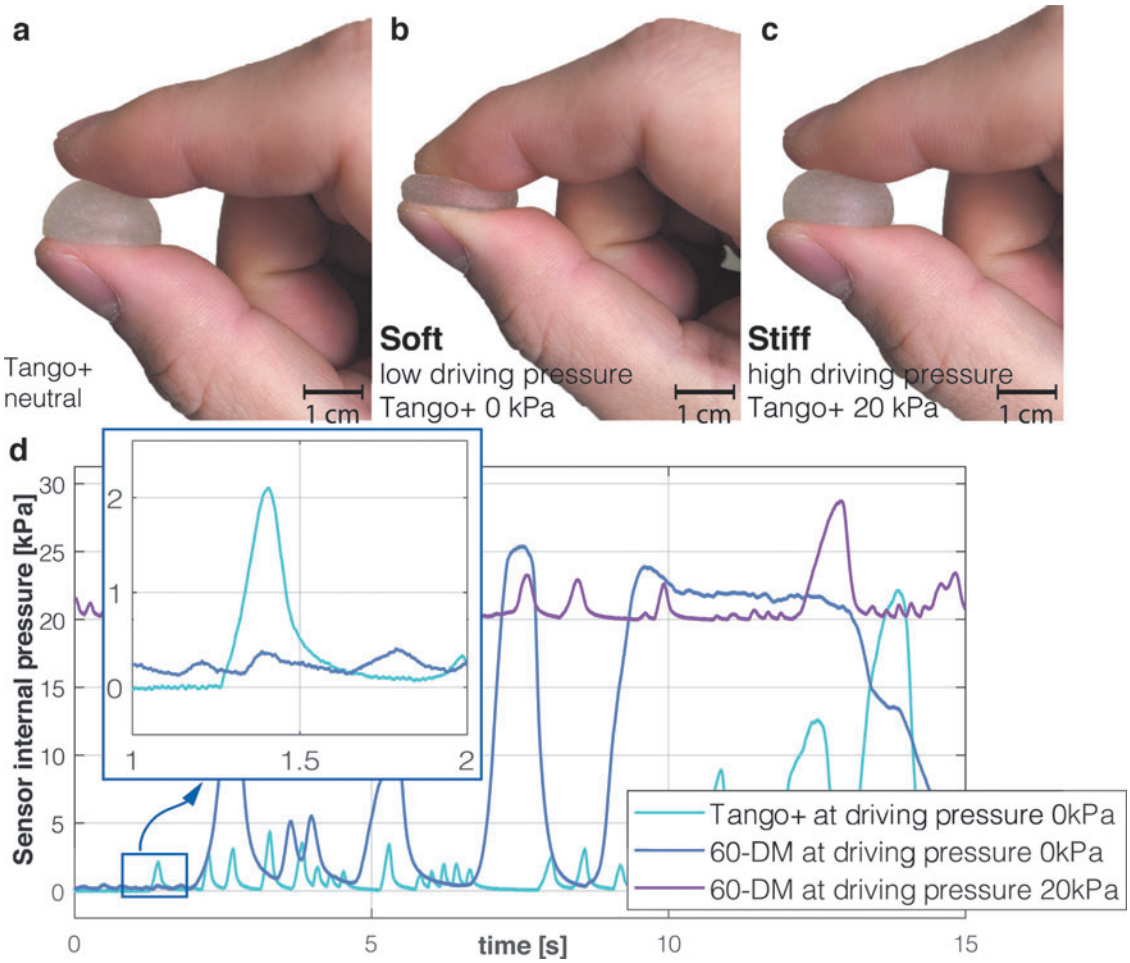

FIG. 1. **(a)** A 3D printed soft sensor with Tango+ without contact and pressurization. **(b)** A 3D printed soft sensor with Tango+ under compression with driving pressure of 0 kPa. **(c)** A 3D printed soft sensor with Tango+ under compression with driving pressure of 20 kPa. **(d)** Sensor response with external force applied for a 3D printed soft sensor with Tango+ under 0 kPa driving pressure, a 3D printed soft sensor with 60-DM under 0 kPa driving pressure, and a 3D printed soft sensor with 960-DM under 20 kPa driving pressure. A zoomed view of the detailed sensor response is shown. The sensor response was recorded at 10 kHz. 3D, three-dimensional; DM, digital materials. Color images are available online.

driving pressure and contact status. h is the distance to the membrane from the origin. When the driving pressure P is equal to P_0 (atmospheric pressure), the sensor is considered as a hemispherical membrane with an uninflated radius R_0 ($h_0 = R_0$) and initial thickness t_o(state 0, Fig. 2).

Considering that the sensor is driven by a positive internal pressure P_I ($P_I > P_0$), state I is inflated to a spherical cap with the height of h_I and base radius of R_0 (Figure 2-I). State II is considered when a rigid surface is coming in contact and pressing the sensor symmetrically (Fig. 2-II). Constant curvature of the noncontact part of the sensor membrane is considered with an assumption of the curvature tangential to the contact surface during the deformation. The membrane of the sensor is modeled as homogeneous, isotropic, and incompressible material.[20]

The principal stretch ratios for the membrane are defined as λ_ϕ, λ_ψ, and λ_t, where λ_ϕ and λ_ψ are for the lateral directions and λ_t is the stretch ratio normal to the membrane.

TABLE 1. MATERIAL PROPERTIES

Material type	*Tango+*	*40-DM*	*50-DM*	*60-DM*	*70-DM*	*85-DM*	*95-DM*
Shore A (STD)	27.6 (1.0)	38.5 (1.5)	50.4 (1.6)	59.9 (2.0)	68.9 (1.4)	80.4 (1.6)	91.3 (2.1)
Shore A -after 1 year (STD)	29.5 (1.8)	42.4 (1.8)	51.1 (1.8)	60.5 (1.5)	68.2 (1.2)	76.0 (1.5)	87.0 (1.8)
p-Value	<0.01	<0.01	0.2112	0.2648	0.0556	<0.01	<0.01
Shore A change	−6.61%	−9.2%	−1.37%	−1.03%	0.99%	5.8%	4.98%
Shear modulus (MPa)	0.17	0.27	0.55	0.91	1.64	4.00	5.33

The *p*-value is calculated with one sample and paired-sample *t*-test for the measured shore A hardness before and after 1 year, testing the null hypothesis that the pairwise difference between the two measurements has a mean equal to zero. In this study, the density of all the materials is modeled as 1.15 g/cm^3 with the Poisson's ratio of 0.49.

DM, digital materials.

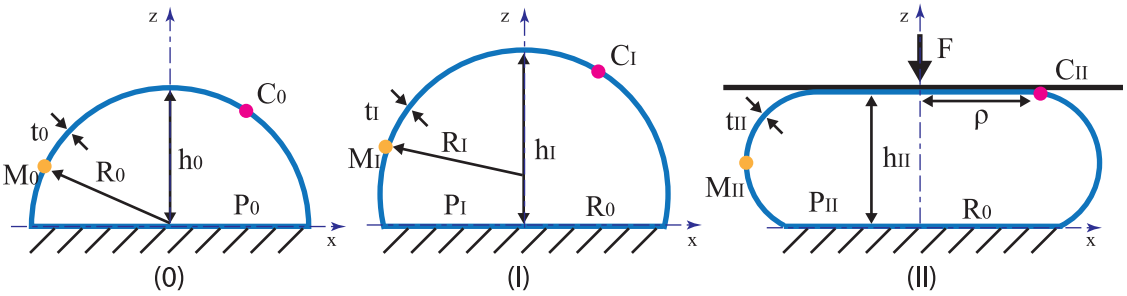

FIG. 2. Theoretical modeling of the sensor. State 0 is the neutral state of the sensor with internal driving pressure equal to atmospheric pressure. State I is the pressurized state where the internal driving pressure is subjected to a positive pressure higher than the atmospheric pressure. State II is the state where the sensor is subjected to external load when interacting with a solid body. The material points of the membrane are defined with points M_0, M_I, and M_{II} for the three states, respectively. The extent of contact during the interaction is characterized by the radius of the contact ρ, shown with material point C_{II} at the edge of contact in the deformed membrane. Color images are available online.

The right Cauchy–Green deformation tensor first and third principal invariant with incompressibility condition[20] are given by:

$$I_1^C = \lambda_t^2 + \lambda_\phi^2 + \lambda_\psi^2 \tag{1}$$

Assuming the silicone membrane material is incompressible with equibiaxial deformation $\lambda_\phi = \lambda_\psi$, the principal stretch ratios are determined by:

$$\lambda_t \lambda_\phi \lambda_\psi = 1 \tag{2}$$

$$\lambda_t = \frac{1}{\lambda_\phi^2} = \frac{1}{\lambda_\psi^2} = \frac{t_1}{t_0} = \lambda_I \tag{3}$$

Where λ_I denotes the normal stretch ratio from state 0 to state I. The volume of the fluid V_g within the sensor cavity is obtained:

$$V_g = \tfrac{1}{6}\pi h_I\left(3{R_0}^2 + {h_I}^2\right) \tag{4}$$

Considering constant volume of the membrane $V_m = V_{mI} = V_{m0} = 2\pi {R_0}^2 t_0 = \pi\left({R_0}^2 + {h_I}^2\right)t_I$

$$\lambda_I = \frac{2{R_0}^2}{\left({R_0}^2 + {h_I}^2\right)} \tag{5}$$

The total potential energy E_p can be expressed as:

$$E_p = \int p dV_g + \int w dV_m \tag{6}$$

Taking the assumption of neo-Hookean material, the strain energy density function:

$$w = C_1\left(\lambda_I^2 + 2\lambda_I^{-1} - 3\right) \tag{7}$$

Thus,

$$E_p = -p\tfrac{1}{6}\pi h_I\left(3{R_0}^2 + {h_I}^2\right) + 2\pi {R_0}^2 t_0 C_1\left(\lambda_I^2 + 2\lambda_I^{-1} - 3\right) \tag{8}$$

Applying the principle of steady state minimum total potential energy, assuming h_I and p are only system variables, h_I can be solved with $\frac{\delta E_p}{\delta h_I} = 0$. The driving pressure p can be expressed by $p_I = k(h_I)$. Considering that the nonlinear function k also depends on the types of hyperplastic material model being used to obtain the strain energy function, neo-Hookean material model is represented with reduced system order to visualize the relation of the sensor geometry to the driving pressure and material stiffness.

$$p_I = k(h_I, C_1) \tag{9}$$

Figure 3a shows the theoretical simulation of the sensor during continuous inflation from state 0 to state I. The sensor exhibits a clear maximum driving pressure during the inflation due to the material hyperelasticity.[21] This ''snap buckling'' behavior is commonly observed in many rubber-like materials where a punctuated reduction of pressure can be observed once it reaches the peak internal pressure.[21,22] The ''snap buckling'' effect happens when the sensor height h_I approaches 17.4 mm based on the given sensor geometry ($R_0 = 9.25\ mm,\ t_0 = 1.5\ mm$). This peak h_I at the maximum driving pressure value is only affected by the original sensor diameter regardless of the membrane stiffness. However, softer material used for the sensor is subjected to larger volume change under the same driving pressure.

A linear relationship between sensor diameter R_0 and peak h_I can be observed, while the result shows no difference between Tango+ and 70-DM (Fig. 3c). Ogden model (parameters from Abayazid and Ghajari[25]) was also used to do a comparison to the neo-Hookean model, with neglected difference exhibited before the sensor reaches the peak h_I (Fig. 3b). For the ease of sensor characterization and modeling, the sensor is only evaluated before it reaches the maximum driving pressure (peak h_I).

State I to state II is modeled by assuming an object with an infinite area exerting an applied force F and a displacement $\Delta\delta = h_I - h_{II}$. The deformation of the membrane is modeled as an asymmetric discotic spherocylinder (Figure 2c).

Assuming 2D axisymmetric revolution and the axis origin at the base center of the sensor, the volume of cavity is:

$$V_{gI} = \int_0^{h_{II}} \pi[\xi(z)]^2 dz \tag{10}$$

Where z represents the distance to the material point of the sensor membrane in the z coordinate and the function $\xi(z)$ represents the x coordinate of the material point given by

$$\xi(z) = \sqrt{\left(\frac{{h_{II}}^2 - (R_0-\rho)^2}{2h_{II}}\right)^2 + (R_0-\rho)^2} - \left(z - \frac{{h_{II}}^2 - (R_0-\rho)^2}{2h_{II}}\right)^2 + \rho \tag{11}$$

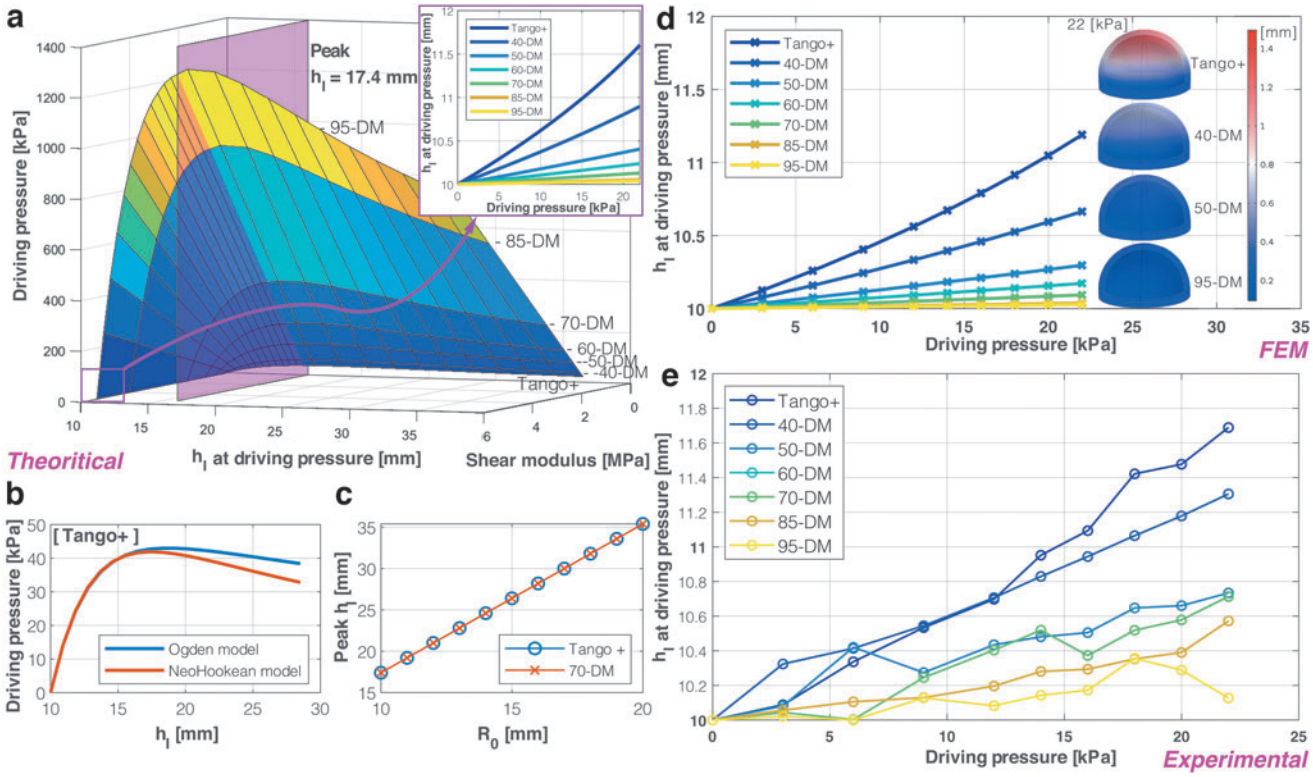

FIG. 3. Theoretical model, FEM simulation, and experimental characterization of the soft sensors from state 0 to state I. **(a)** theoretical modeling of the sensor under continuous inflation with Tango+ and all DM. Neo-Hookean model with shear modulus used in Table 1 indicates the material stiffness. A clear ''snap buckling'' behavior can be observed during the inflation with the peaks always exhibiting when $h_I = 17.4$ mm regardless of the membrane stiffness. The ''snap buckling'' presents with the maximum driving pressure, as it increases with the increase of membrane stiffness. The lowest maximum driving pressure with the sensor made from Tango+ is around 42 kPa. A zoom view of the sensor geometry change (theoretical) is also presented between driving pressure 0 to 22 kPa. **(b)** Comparing the Ogden hyperplastic material model of Tango+ obtained from Abayazid and Ghajari[25] with the neo-Hookean material model. **(c)** The theoretical model indicates that the peak h_I at the ''snap buckling'' point exhibits a linear relation to the size of the sensor. However, the peak h_I is independent of the material stiffness. **(d)** The geometry changes of the soft sensors with increased driving pressure, results from FEM. The deformation of the sensors made from Tango+, 40-DM, 50-DM, and 95-DM at the driving pressure of 22 kPa is shown. The color bar indicates the deformation in mm. **(e)** The geometry changes of the soft sensors with increased driving pressure, results from experimental characterizations. FEM, finite element modeling. Color images are available online.

Considering constant material volume of the membrane with the assumption of incompressibility:

$$\pi\left(R_0^2 + h_I^2\right)t_I = \pi\rho^2 t_{II} + 2\pi\int_0^{h_{II}} \xi(z)\sqrt{1+\left[\xi'(z)\right]^2}\,dz t_{II} \tag{12}$$

Thus,

$$\lambda_{II} = \frac{t_{II}}{t_I} = \frac{\pi\left(R_0^2 + h_I^2\right)}{\pi\rho^2 + 2\pi\int_0^{h_{II}} \xi(z)\sqrt{1+\left[\xi'(z)\right]^2}dz} \tag{13}$$

Again, consider the minimum total potential energy principle and the neo-Hookean model:

$$E'_p = -p_{II}V_{gt} + 2\pi R_0^2 t_0 C_1\left(\lambda_{II}^2 + 2\lambda_{II}^{-1} - 3\right) - F\Delta\delta \tag{14}$$

Assume Boyle's law pv is constant,

$$(p_{II} + p_m)V_{gt} = (p_I + p_m)V_g \tag{15}$$

the applied force is determined by:

$$F = p_{II}\,\pi\rho^2 \tag{16}$$

then

$$E'_p = -p_I V_g + 2\pi R_0^2 t_0 C_1\left(\lambda_{II}^2 + 2\lambda_{II}^{-1} - 3\right) - \left(\frac{(p_I + p_m)V_g}{V_{gt}} - p_m\right)\pi\rho^2(h_I - h_{II}) \tag{17}$$

Substituting (10) and (13) into (17), assuming $\frac{\delta E'_p}{\delta h_{II}} = 0$ under the boundary condition $0 < \rho < R$.

The increase of pressure and force can be obtained with the following nonlinear equations:

$$\Delta p = f(p_I,\ \Delta\delta) \tag{18}$$

And,

$$F = \varphi(p_I, \Delta\delta) \tag{19}$$

Finite element modeling

Finite element modeling (FEM) with COMSOL 5.3a is used in the study to simulate the soft sensor physical behavior under positive pressure and estimate the change of sensing characteristics reflected by internal pressure variations. In contrast to the membrane model used in the theoretical simulation, the FEM is determined with a solid mechanics model to reveal the contribution of structural stiffness. The FEM simulation is performed in two studies: (1) the sensor is pressurized freely with a defined driving pressure from state 0 to state I, and (2) a rigid indenter is introduced in state II to exert regulated loading with step control. In study 2, the internal pressure is solved based on the result of study 1 and the governing sensor deformation. See Supplementary Data B for details of the simulation setup.

Experimental Characterization

Characterization setup

The sensor experimental characterization was conducted with a 3-axis Cartesian robot, performing indentation tests against a flat surface with the sensor mounted on the indenter (Fig. 4). Details about the setup and data acquisition can be found in Supplementary Data C.

Sensitivity and repeatability

To evaluate the sensitivity and repeatability of the sensor, the characterization is conducted with robot position control. The probe moved along the z-axis to a specified z-position and stayed at the position for 4 s, and it returned to the initial no-contact position. A step-increment (0.5 mm step) indentation was repeated until the sensor reached the defined maximum deformation (three-quarters of the original sensor radius R_0 to avoid damage). We repeated this test three times for seven soft tactile sensors (Tango+, 40–95 DM) at each driving pressure ($\sim$450 indentations for each sensor). Between each indentation, we waited 30 s and reset the pressure value to remove any hysteresis effect. The sensitivity S of the sensors is defined as $\Delta P/\Delta F$, where ΔP is the internal pressure variation and ΔF denotes the applied force.

Saturation, sensing range, and hysteresis

Previous tests set the maximum deformation as three quarters of the sensor radius. In this part, we tested the soft sensor until it saturates. The sensing range and hysteresis are also evaluated with this test. All sensors (Tango+, 40–95 DM) were tested with a comparison between driving pressure 0 *kPa* (soft state) and 12 *kPa* (stiff state). The tests were performed with the same load-unload pressure cycle, as mentioned previously. However, the waiting time between each indentation was reduced to 2 s, and the internal pressure was not reset.

Results and Discussion

In the following section, we compared the results from the theoretical study (solved numerically with Matlab 2020a), FEM simulation, and empirical characterization. The sensor stress relaxation, manufacturing repeatability, and the effect of aging are also experimental tested (Supplementary Data D and E).

Tunable stiffness

The sensor stiffness is the contribution of structural stiffness and pressurization of the sensor cavity. The theoretical model focused mainly on the effect of pressurization with a membrane assumption, while the FEM simulation represents

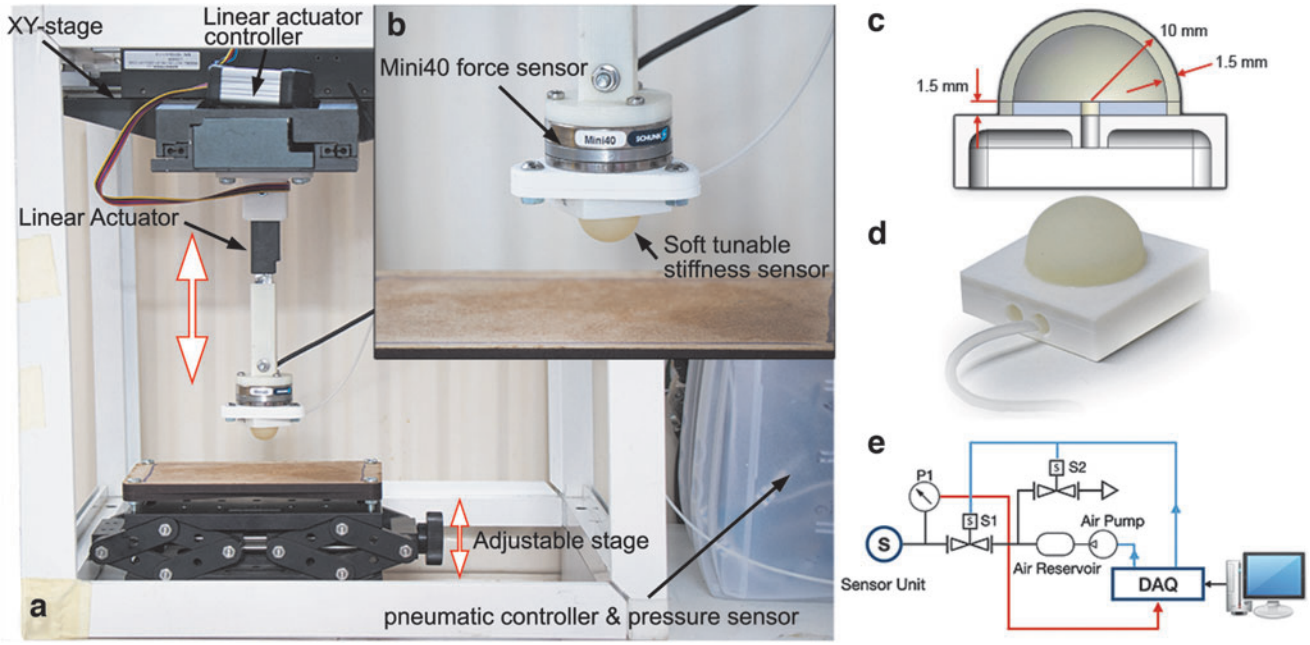

FIG. 4. Setup for the sensor characterization. **(a)** The indentation setup with a Cartesian robot. **(b)** A closer view of the soft sensor mounted on the indenter. **(c)** Schematics and dimensions of the soft sensor. **(d)** The 3D printed soft sensor is mounted on a rigid connector (ABS, 3D printed) for testing. **(e)** The pneumatic connection diagram to control the sensor driving pressure and record the internal pressure variation. Color images are available online.

both contributions. Results of theoretical model, FEM, and experimental characterization are reported in Figure 5a–c, respectively.

A clear increase of the stiffness can be observed with the increase of indentation depth denoting the nonlinear mechanical property. The stiffness (shown in Fig. 5a) is defined as $dF/d\Delta h$, where F is the applied load on the soft sensor and Δh is the indentation depth. Results from the theoretical model indicate that the increase of driving pressure would increase the sensor stiffness before the driving pressure reaches the maximum driving pressure where $h_I = 17.4\ mm$. With further inflation, the sensor stiffness drops after the maximum driving pressure is reached, representing the membrane "snap buckling."

Thus, we define the pressure region lower than maximum driving pressure as the valid pressure-based control region for tunable stiffness. FEM and experimental results also validate the feasibility of controlling sensor stiffness with internal driving pressure. However, it needs to be noted that when the material stiffness is increased, the required change on driving pressure to increase the internal driving pressure is also increased significantly due to the increased structural stiffness.

Sensitivity and repeatability

The sensitivity S of the sensors is defined as $\Delta P/\Delta F$, where ΔP is the internal pressure variation and ΔF denotes

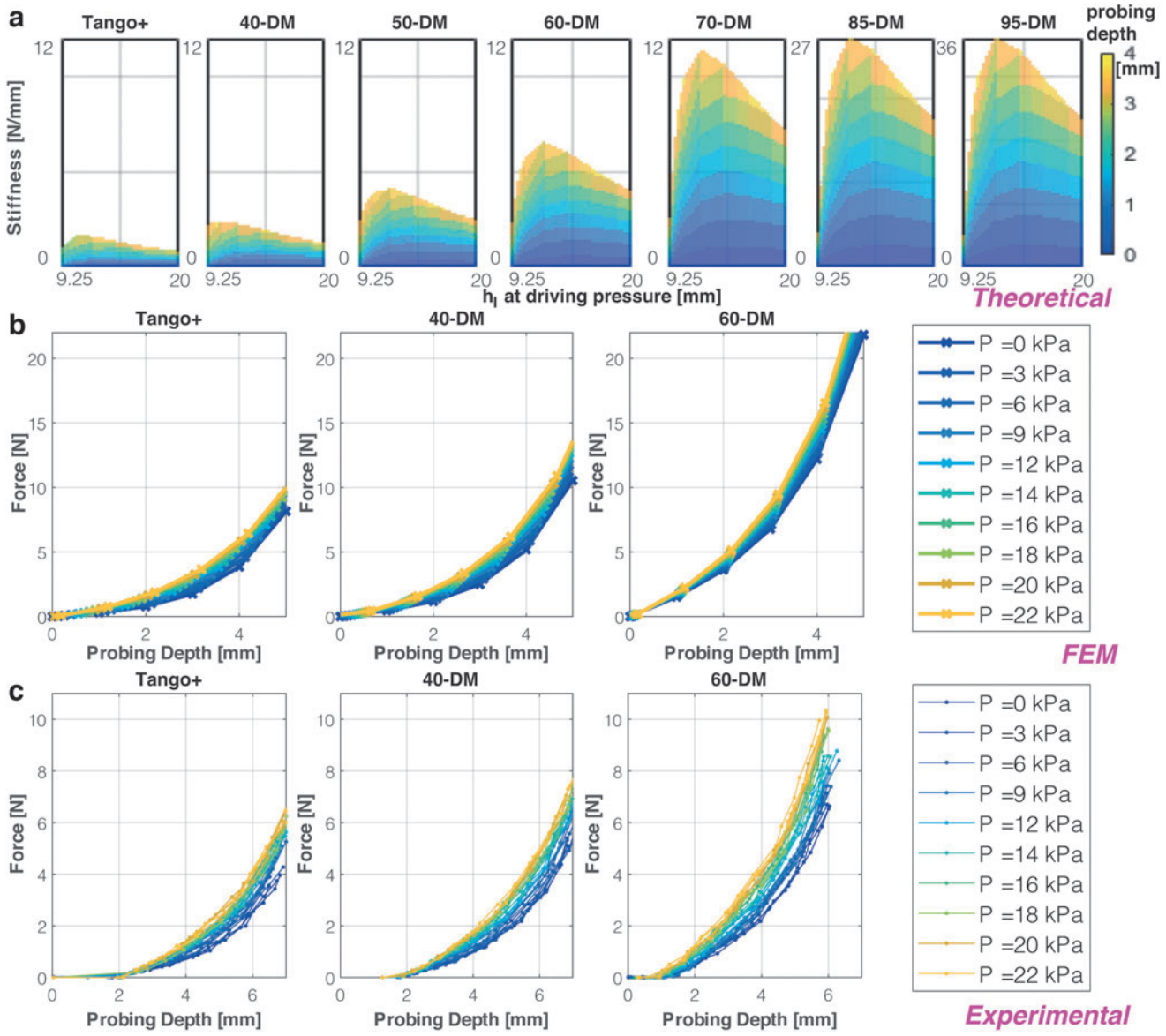

FIG. 5. Selected results of sensor mechanical property change with both online (driving pressure) and offline (membrane stiffness) parameters. **(a)** The theoretical modeling result. The color bar indicates the probing depth of the indentation. The x-axis is the geometry data of the sensor with h_I (state I) at a specific driving pressure. The y-axis is the sensor stiffness characterized by $dF/d\Delta h$. **(b)** The result from FEM studies. Indentation force with probing depth for sensors with increased driving pressure. **(c)** The result from experimental characterization. Indentation force with probing depth for sensors with increased driving pressure. All three-trial data on three identical sensors for each driving pressure are shown in the subplot for Tango+, 40-DM, and 60-DM. Good repeatability of all sensors can be observed. The full set results for all materials can be found in Supplementary Figure S3. Color images are available online.

the applied force. The result of FEM simulation shows the change of the internal pressure and applied force at each indentation depth (Fig. 6a). Selected detailed result with a clear linear relation of the sensitivity is shown in Figure 6d–f. The estimated sensitivity with a linear model is shown in Figure 6g. Sensors made from soft material Tango+, 40-DM, 50-DM, 60-DM show a decrease in sensitivity with the increase of driving pressure, while sensors made from stiff material exhibit a slight increase in sensitivity with increased driving pressure. Sensor made from 70-DM shows neglected change in sensitivity up to the driving pressure of 22 kPa. For Full results see Supplementary Data F.

The theoretical result (Fig. 7a) shows decreases in the sensitivity for the soft sensors with increased driving pressure. However, minimum sensitivity region can be observed in the model. This minimum region is assumed to happen when the driving pressure is approaching the maximum pressure, while a slight increase of sensitivity exhibits after the snap-through. The model also indicates high linearity of the sensor response between ΔP and ΔF, with R squared values reported in Figure 7b.

The experimentally characterized sensor responses under different driving pressures are reported in Figure 7c–e for sensors fabricated with Tango+, 40-DM, and 60-DM, respectively. Good linearity can also be observed for sensors within the tested force range (determined as a maximum of three-quarters of the sensor radius).

The highest sensitivity case $S = 2.6$ KPa/N happens at the softest tactile sensor fabricated by tango+ under the lowest driving condition. By increasing the material stiffness, the sensitivity also drops monotonically, in which the trend is aligned with the FE simulation result and mathematical

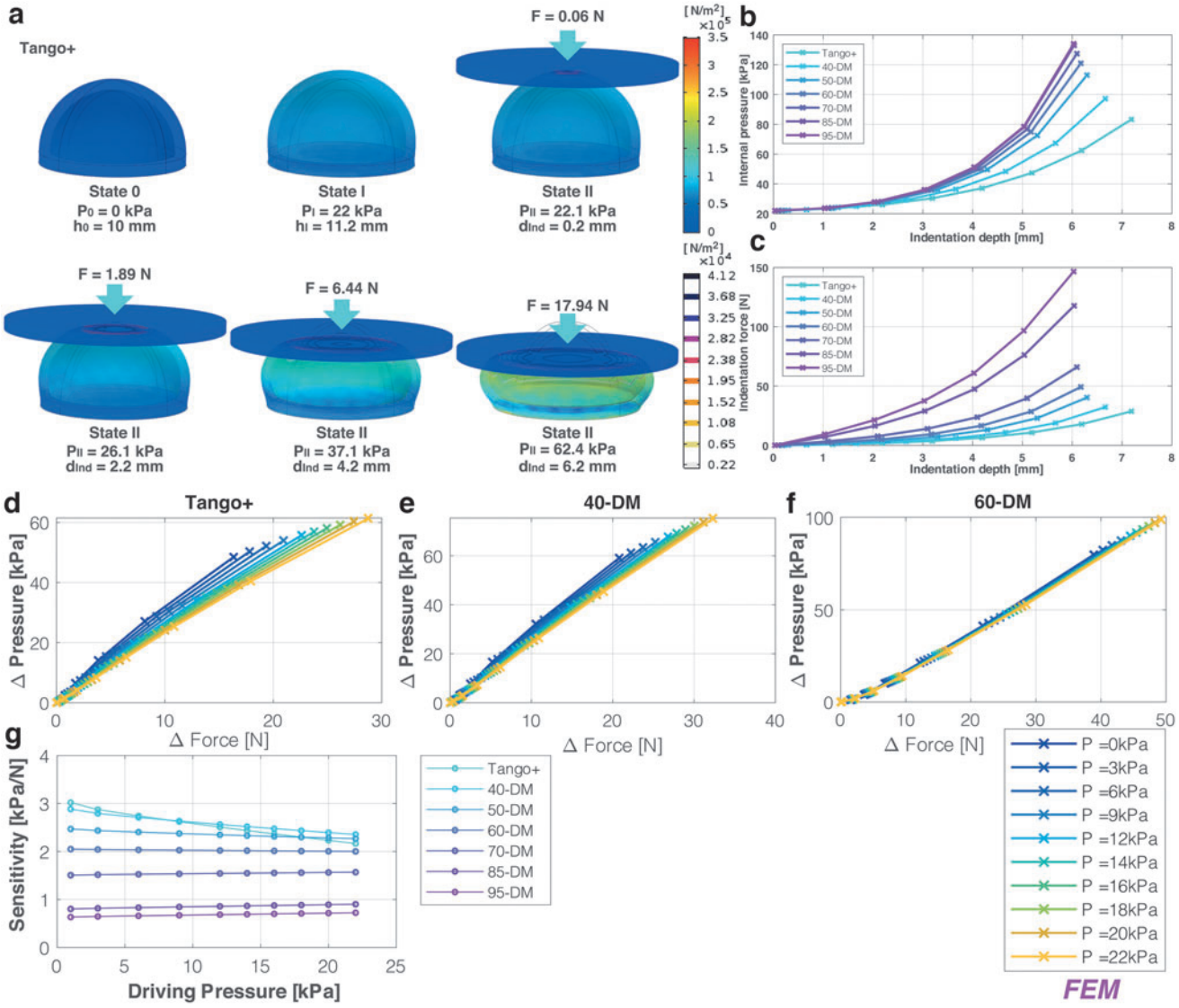

FIG. 6. Selected sensitivity results from the FEM study. **(a)** Result of the sensor made from Tango+ under 22 kPa driving pressure, from state 0, I to II. The deformation, the von Mises stress on the surface, and the contact pressure are shown. **(b, c)** Internal pressure and force data for all sensors made from different materials at the driving pressure of 22 kPa. **(d–f)** The results of sensor response ΔP at different applied forces ΔF are shown in **(d–f)** for membrane materials of Tango+, 40-DM, and 60-DM, respectively. **(g)** The overall sensitivity changes of the soft sensors made from different materials with increased driving pressure. The full set results for all materials can be found in Supplementary Figure S4. Color images are available online.

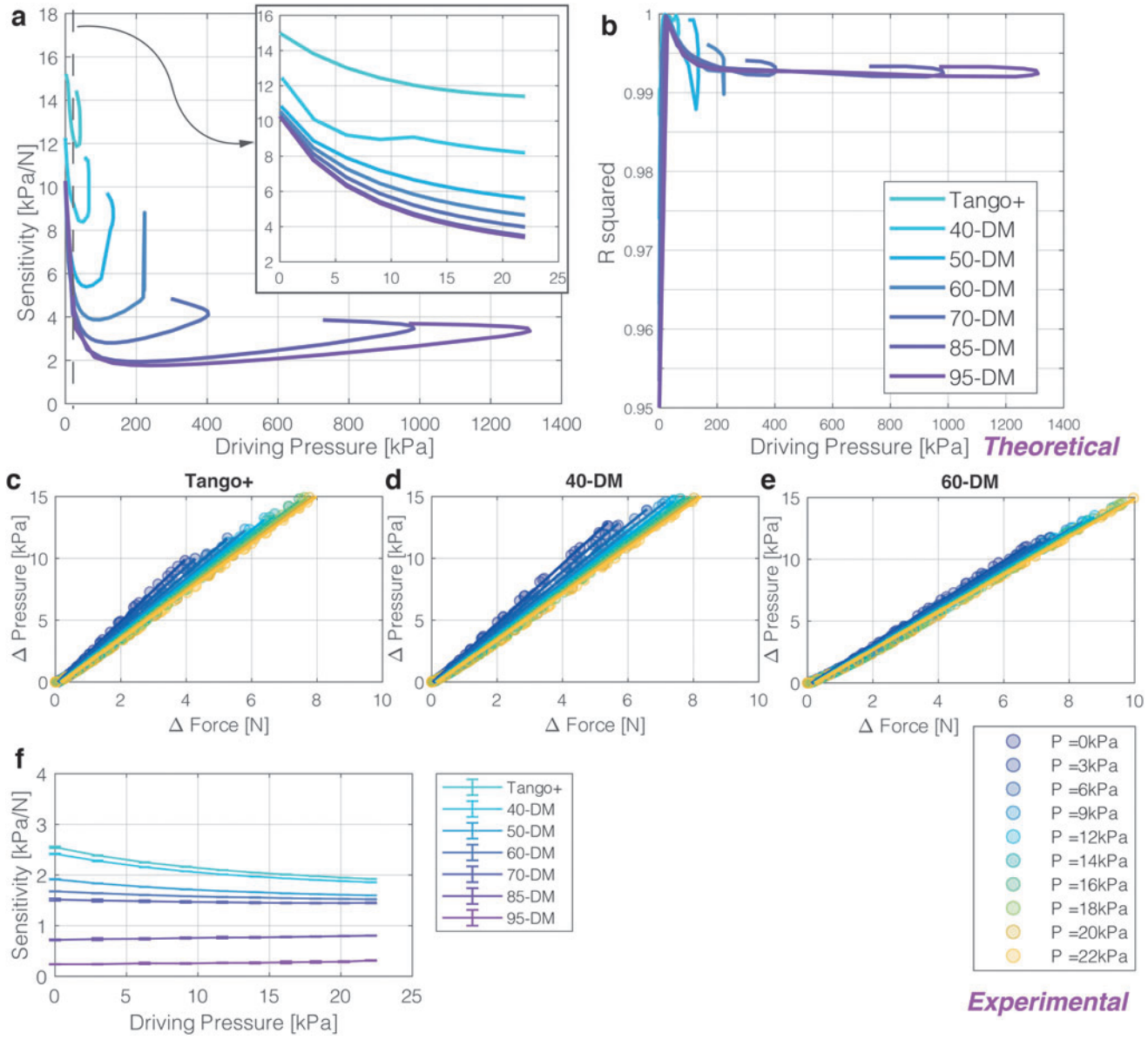

FIG. 7. **(a)** Theoretical result of the sensor sensitivity change with increased driving pressure. A zoom view of the experimental tested low-pressure (<22 kPa) region is shown. Part of the curve shows two sensitivity values due to the existence of material ''snap bulking.'' During inflation, the membrane will continue to increase its volume after the maximum pressure is reached, yet with reduced internal pressure. **(b)** Linearity of the sensor response with ΔP and ΔF is represented with R squared value at each driving pressure. **(c–e)** Selected experimental sensor response with the three trials of repetition on identical sensor samples for sensor made from Tango+, 40-DM, and 60-DM. A linear model is used to fit the sensor response. **(f)** The overall sensitivity changes of the soft sensors made from different materials with increased driving pressure. Standard deviation error shown for repeated tests on three identical samples. Average STD for Tango+ and 40–95 DM are 0.0051, 0.0035, 0.0022, 0.0035, 0.0138, 0.0109, 0.0108, respectively. The average STD for all sensors is 0.0071. The full set results for all materials can be found in Supplementary Figure S5. Color images are available online.

model. It can be noticed that experimental and FEM simulation results show different absolute values in sensitivity with an average error of 37.94% at the driving pressure of 0 kPa and an average error of 37.96% at the driving pressure of 22 kPa. Sensor made of 70-DM shows the smallest difference of the results with an average error of 3.81% between the driving pressure of 0 to 22 kPa. Sensor made of 95-DM shows the largest error among all the samples.

As anticipated, this difference results from the specific characterization of the material sample. The material values are obtained from literature, and it is known that there can be differences between different samples of the same material. In addition, the experimental characterization may also experience factors that are idealized in the FEM simulation, for instance, the friction during the indentation. It also needs to be noted that although the value of the sensitivity from the theoretical model is not as accurate as the experimental and FEM result, a similar trend can still be observed. The difference presumably results from the idealized modeling of the soft membrane.

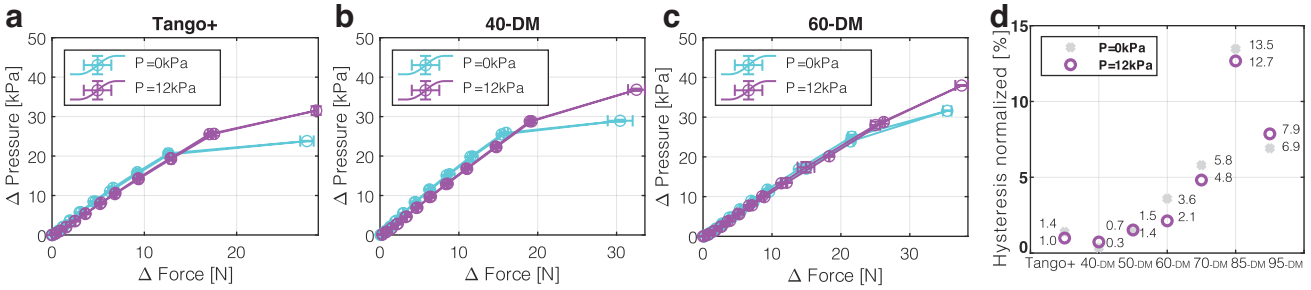

FIG. 8. Selected result of continuous loading tests. The result of sensors made from Tango+, 40-DM, and 60-DM is shown in **(a–c)**, respectively. All sensors are tested in three trials with the driving pressure of 0 and 12 kPa. Sensors are tested upon saturation during the test. **(d)** Normalized hysteresis. The full set results for all materials can be found in Supplementary Figure S6. Color images are available online.

Overall, for tactile sensors that were fabricated by a softer material (Tango+, 40-DM), the sensitivity drops when the internal driving pressure increases. However, for tactile sensors fabricated by stiffer material such as 85-DM and 95-DM, the sensitivity increases with the increase of internal driving pressure. This is due to the fact that the material is so stiff that the increase of sensor stiffness caused by an increase of internal pressure is too small compared to the material stiffness. Thus, the increase of stiffness can be neglected unless the sensor is pressurized to a much higher region.

Without the contribution of material stiffness, the sensor is more sensitive at higher pressurized conditions. By contrast, the drop of sensitivity at higher pressurized conditions for soft sensors caused by the increase of sensor stiffness (less strain deformation for the same amount of stress) compensates this increase of sensitivity caused by an increase of internal driving pressure. The two phenomena fully compensate each other for sensor fabricates by 70-DM, where a flat line of sensitivity can be observed in Figure 7f for the specific sensor. This behavior is in alignment with the FEM simulation in Figure 6g. Figure 7j also included the standard deviation of the sensitivity in three trials of characterization, where excellent repeatability can be observed (average std <0.008).

Saturation, sensing range, and hysteresis

The experimental results in Figure 8 show the sensor response under repeated loading conditions upon saturation with two selected driving pressures (0 and 12 kPa). The

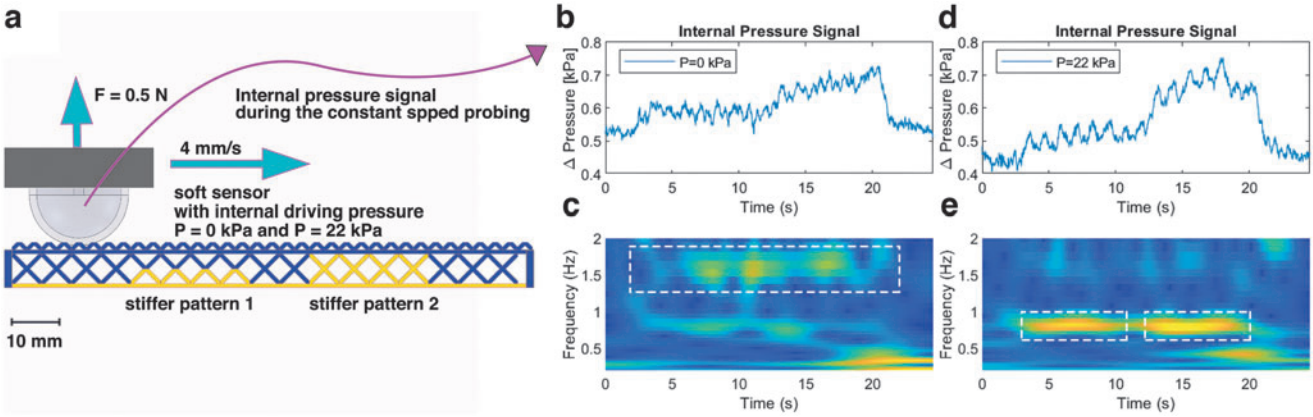

FIG. 9. **(a)** The online tunable stiffness of the sensor is tested by detecting the texture of a multilayer lattice structure. The sensor (fabricated with Tango+) is being inflated to two states during the tactile exploration. The driving pressure $p = 0$ kPa for the soft state. The driving pressure $p = 22$ kPa for the stiff state. The sensor is first applied to the structure with the normal force of 0.5 N for both states and then moved with a constant speed of 4 mm/s to detect the texture in the multilayer lattice structure. PTFE lubricant is applied to the sensor surface to reduce friction. The multilayer lattice structure (3D printed with J735; Stratasys Ltd.) is made of two materials. The *dark-region* material (Agilus30 is a soft and rubber-like material with a quoted tensile strength of 2.1–2.6 MPa and Shore hardness of 30 A, Stratasys Ltd.) and the *light-region* material (Vero is a rigid plastic-like material with a quoted tensile strength of 50–65 MPa and a Shore hardness of 83–86D). The distance of the higher frequency surface pattern is around 3 mm. The distance of the lower frequency buried pattern is around 6 mm. Considering the probing speed of 4 mm/s, the computed baseline frequency for the lower frequency pattern is around 0.75 Hz, and the computed baseline frequency for the lower frequency pattern is around 1.5 Hz. **(b)** The internal pressure signal during the detection at its soft state with 0 kPa driving pressure (signal recorded at 10 kHz). **(d)** The internal pressure signal during the detection at its stiff state with 22 kPa driving pressure (signal recorded at 10 kHz). **(c)** The result of the continuous wavelet transform of the soft state sensor signal. A sharper detection of the higher frequency surface structure is found around 1.5 Hz. **(e)** The result of the continuous wavelet transform of the stiff state sensor signal (analytic Morse wavelet). A sharper detection of the lower frequency buried structure is found around 0.75 Hz. Both stiffer patterns 1 and 2 are detected with a sharper detection of pattern 2. Color images are available online.

sensing range increased with the increase of driving pressure. This effectively solved the issue that many soft sensors are only sensitive at a low-force region while getting easily saturated when the force increases.

In addition, the sensors made from Tango+, 40-DM, 50-DM, 60-DM, and 70-DM exhibit neglected hysteresis (<6%). The hysteresis is considerably low compared to many piezoresistive,[26] capacitive[3] sensors and sensors made of conductive rubber[27] reported from literature.[1] Together with the high-frequency sampling rate (10 kHz), the sensor shows good potential in dynamic interaction. Indeed, the sensor hysteresis increases with the increase of material stiffness. The hysteresis for the stiff sensors made from 85-DM and 95-DM is still considerably low (<14%) compared to conductive polymer-based soft sensors. For Full results see Supplementary Data F.

Online Tunable Stiffness in Soft Texture Detection

To demonstrate the advantage of tuning the sensor stiffness during tactile exploration, a soft sensor (Tango+) is used to detect the texture of a multilayer lattice structure. The experiment is performed with the same setup introduced in Supplementary Data C. Figure 9a shows the experimental protocol with the multilayer lattice structure being examined. The sensor is first inflated up to the defined driving pressure (0 kPa as the soft state and 22 kPa as the stiff state) and then performs an indentation with the normal force equal to 0.5 N. The texture is then detected by probing the lattice structure with the sensor at a constant speed of 4 mm/s.

The internal pressure signal during the probing is shown in Figure 9b and d. By analyzing the sensor response in the frequency domain with a continuous wavelet transform, the result shows a significant change for the same sensor at its soft and stiff state (Fig. 9c, e). Although the applied force is the same for both states, the sensor at soft state shows a sharper distribution in detecting the higher frequency surface texture, while the sensor at stiff state shows a better performance in detecting the lower frequency texture. Figure 9e shows a clear distribution of both regions of buried texture with a sharper detection of the stiffer pattern 2 since it is closer to the surface. This experiment demonstrates the use of online sensor stiffness tuning in better detecting various features compared to sensors with only fixed characteristics.

Conclusions

In this article, we show that tunable stiffness soft sensors help to estimate task-relevant states while filtering others. Pneumatic-based soft sensing with elastomeric materials is promising due to the low cost of pressure sensors, compact size, and ease of integration in soft robotic systems. Controlling the mediating fluid of such a sensor allows it to favor its sensing characteristics to adapt to the environment as an online parameter. If a soft sensor is only implemented with a fixed sensitivity and mechanical property, multiple sensors with different sensing characteristics are commonly needed to detect different features. For instance, Interlink's commercial tactile sensors are developed with different sensing ranges (0.2 to 20 N, 0.3 N to 50 N, and 0.5 N to 150 N). Creating tunable contact dynamics in specific tasks also requires the assembly of filters to a fix-property sensor.

Indeed, the proposed sensor can be designed in many shapes and dimensions. We choose to test the sensor by fabricating it in the hemispherical shape for the purpose of ease on generalization, modeling, and characterization (demonstrated in the Supplementary Video S1). A theoretical model with membrane assumption, FEM with neo-Hookean solid mechanics simulation, and experimental characterization all validate the feasibility to tune the sensor mechanical property and sensing characteristics with the combination of online and offline parameters.

This study opens up new opportunities to integrate 3D printed soft sensors for active perception. In contrast to passively relying on the static tactile information from sensors that have large variability during soft interaction, the new direction of active perception can actively decode the tactile information by tuning its sensitivity and specificity with a tunable physical reservoir that filters the signal. In future studies, we will focus on the application of active sensing with the tunable stiffness soft sensors in stiffness discrimination, texture recognition, and designing the soft sensors in more diverse geometries to be integrated with other soft robotic systems.

Author Disclosure Statement

No competing financial interests exist.

Funding Information

This work was supported by the Engineering and Physical Sciences Research Council (EPSRC) Programme Grant EP/V000748/1 from Sensing to Collaboration: Engineering, Exploring and Exploiting the Building Blocks of Embodied Intelligence and RoboPatient grant EP/T00603X/1.

Supplementary Materials

Supplementary Data A
Supplementary Data B
Supplementary Data C
Supplementary Data D
Supplementary Data E
Supplementary Data F
Supplementary Video S1

References

1. Dahiya RS, Metta G, Valle M, *et al.* Tactile sensing—From humans to humanoids. IEEE Trans Robot 2009;26:1–20.
2. Lee MH, Nicholls HR. Review Article Tactile sensing for mechatronics—A state of the art survey. Mechatronics 1999;9:1–31.
3. Maiolino P, Maggiali M, Cannata G, *et al.* A flexible and robust large scale capacitive tactile system for robots. IEEE Sens J 2013;13:3910–3917.
4. Seminara L, Pinna L, Valle M, *et al.* Piezoelectric polymer transducer arrays for flexible tactile sensors. IEEE Sens J 2013;13:4022–4029.
5. Stassi S, Cauda V, Canavese G, *et al.* Flexible tactile sensing based on piezoresistive composites: A review. Sensors 2014;14:5296–5332.
6. Zhao H, O'Brien K, Li S, *et al.* Optoelectronically innervated soft prosthetic hand via stretchable optical waveguides. Sci Robot 2016;1:eaai7529.
7. Wang H, Totaro M, Beccai L. Toward perceptive soft robots: Progress and challenges. Adv Sci 2018;5:1800541.
8. Schmitz A, Maiolino P, Maggiali M, *et al.* Methods and technologies for the implementation of large-scale robot tactile sensors. IEEE Trans Robot 2011;27:389–400.

9. Alspach A, Hashimoto K, Kuppuswamy N, *et al.* Soft-bubble: A highly compliant dense geometry tactile sensor for robot manipulation. In 2019 2nd IEEE International Conference on Soft Robotics (RoboSoft 2019). Seoul, Korea: IEEE, 2019, pp. 597–604.
10. He L, Lu Q, Abad SA, *et al.* Soft fingertips with tactile sensing and active deformation for robust grasping of delicate objects. IEEE Robot Autom Lett 2020;5:2714–2721.
11. Scimeca L, Hughes J, Maiolino P, *et al.* Action augmentation of tactile perception for soft-body palpation. Soft Robot 2021; DOI: 10.1089/soro.2020.0129.
12. Sornkarn N, Nanayakkara T. Can a soft robotic probe use stiffness control like a human finger to improve efficacy of haptic perception? IEEE Trans Haptics 2016;10:183–195.
13. Sornkarn N, Dasgupta P, Nanayakkara T. Morphological computation of haptic perception of a controllable stiffness probe. PLoS One 2016;11:e0156982.
14. Wegiriya H, Herzig N, Abad SA, *et al.* A stiffness controllable multimodal whisker sensor follicle for texture comparison. IEEE Sens J 2019;20:2320–2328.
15. Herzig N, He L, Maiolino P, *et al.* Conditioned haptic perception for 3D localization of nodules in soft tissue palpation with a variable stiffness probe. PLoS One 2020; 15:e0237379.
16. Thuruthel TG, Hughes J, Georgopoulou A, *et al.* Using redundant and disjoint time-variant soft robotic sensors for accurate static state estimation. IEEE Robot Autom Lett 2021;6:2099–2105.
17. Scimeca L, Maiolino P, Iida F. Efficient Bayesian exploration for soft morphology-action co-optimization. In 2020 3rd IEEE International Conference on Soft Robotics (RoboSoft 2020). New Haven, USA: IEEE, 2020, pp. 639–644.
18. Zou L, Ge C, Wang ZJ, *et al.* Novel tactile sensor technology and smart tactile sensing systems: A review. Sensors 2017;17:2653.
19. He L, Herzig N, de Lusignan S, *et al.* An abdominal phantom with tunable stiffness nodules and force sensing capability for palpation training. IEEE Trans Robot 2021; 37:1051–1064.
20. Holzapfel AG. Nonlinear Solid Mechanics II. Hoboken, New Jersey, USA: John Wiley & Sons, Inc., 2000.
21. Mullins L. Softening of rubber by deformation. Rubber Chem Technol 1969;42:339–362.
22. Ogden RW. Large deformation isotropic elasticity–on the correlation of theory and experiment for incompressible rubberlike solids. Proc R Soc Lond A Math Phys Sci 1972; 326:565–584.
23. Slesarenko V, Rudykh S. Towards mechanical characterization of soft digital materials for multimaterial 3D-printing. Int J Eng Sci 2018;123:62–72.
24. Liu L, Li Y. Failure mechanism transition of 3D-printed biomimetic sutures. Eng Fract Mech 2018;199:372–379.
25. Abayazid FF, Ghajari M. Material characterisation of additively manufactured elastomers at different strain rates and build orientations. Addit Manuf 2020;33:101160.
26. Beebe DJ, Hsieh AS, Denton DD, *et al.* A silicon force sensor for robotics and medicine. Sens Actuators A Phys 1995;50:55–65.
27. Shimojo M, Namiki A, Ishikawa M, *et al.* A tactile sensor sheet using pressure conductive rubber with electrical-wires stitched method. IEEE Sens J 2004;4:589–596.

Address correspondence to:
Liang He
Oxford Robotics Institute
University of Oxford
Oxford OX2 6NN
United Kingdom

E-mail: liang.he@eng.ox.ac.uk